Microfluidics and Nanofluidics (2020) 24:91
https://doi.org/10.1007/s10404-020-02394-8

RESEARCH PAPER

2D acoustofluidic patterns in an ultrasonic chamber modulated by phononic crystal structures

Qiang Tang[1] · Pengzhan Liu[2] · Xin Guo[1] · Song Zhou[1] · Yuwei Dong[1]

Received: 20 July 2020 / Accepted: 5 October 2020 / Published online: 22 October 2020

Abstract

Controllable manipulation of micro/nano-particles and biological organisms are essential for the engineering development of miniaturized lab-on-a-chip systems in the application of physical, chemical, and biological researches. In this paper, a series of phononic crystal structure based acoustofluidic devices, which are actuated by incident plane wave at different frequencies, have been proposed and numerically investigated for micro-particle manipulation. The interaction between different phononic crystal structures and ultrasonic waves, providing reflection, scattering and diffraction, can generate diverse spatial variations of sound field distribution along the wave propagation path. The combination of phononic crystal structures and lab-on-a-chip devices is beneficial to overcome the monotonousness of the acoustofluidic field distribution for various physical and biochemical applications. The movement trajectories of micro-particles under the influence of acoustic radiation forces and acoustic streaming induced drag forces are also simulated to demonstrate the particle manipulation capability of the designed acoustofluidic device. Our simulation results suggest the possibility of considering phononic crystal structures as an effective ingredient to customize acoustofluidic field for constituting diverse lab-on-a-chip devices in the investigation of rapid microfluidic mixing and non-invasive manipulation of bio-organisms.

Keywords Acoustofluidic field · Phononic crystal structure · Sound wave modulation · Micro-particle manipulation

1 Introduction

Integrated microfluidic devices, also known as "lab-on-a-chip" systems (Folch 2012), have achieved increasing attention and played a fundamental role in the field of micro-/nano-scale particle manipulation (Li et al. 2013), biochemical reaction (Ohno et al. 2010), total analysis of bio-samples (Lisowski and Zarzycki 2013), locomotion mechanism of autonomous micro/nanomachines (Lu et al. 2019), point-of-care diagnostics (Frank 2013), and at-home tests for various health issues (Srinivasan et al. 2004), and so on. However, there have been limitations and challenges in the development process, in particular with difficulties associated with the microfluidic chip interconnection to other auxiliary instruments and in the precise and harmless manipulation process of living bio-organisms (Whitesides 2006). For instance, a large proportion of microfluidic driving methods currently used require either external pressure-driven pumps or strong optical/electric/magnetic field, which brings a series of disturbing problems such as loss of valuable samples by imprecision control along the microfluidic channel and irreversible damage of fragile cell membranes and organelles (Stone and Kim 2001; Ehrnström 2002; Temiz et al. 2015).

To provide sufficient driving forces that can overcome the viscous resistance caused by the surrounding media or the adhesive effect at the solid–fluid interfaces and achieve precise control of micro-/nano-scale particles and bio-organisms in a microfluidic chamber, researches worldwide have verified and developed numerous driving and manipulation methods for capturing, transporting, rotating, and separating

Electronic supplementary material The online version of this article (https://doi.org/10.1007/s10404-020-02394-8) contains supplementary material, which is available to authorized users.

✉ Qiang Tang
tangqiang102@126.com

[1] Jiangsu Provincal Engineering Research Center for Biomedical Materials and Advanced Medical Devices, Faculty of Mechanical and Material Engineering, Huaiyin Institute of Technology, Huaian 223003, China

[2] State Key Lab of Mechanics and Control of Mechanical Structures, Nanjing University of Aeronautics and Astronautics, Nanjing 210016, China

of micro-/nano-scale objects (Dalili et al. 2018). Existing active manipulation methods of micro-/nano-scale particles and bio-samples, including mechanical (Jericho et al. 2004), electric/dielectric (Zhou et al. 2018), magnetic/diamagnetic (Reverté et al. 2016), optical (Kotz et al. 2004), thermal (Chen et al. 2016), and acoustic forces (Luong and Nguyen 2010), take advantages of intense driving forces and comparatively high manipulation precision. Conventional passive manipulation techniques, including particle filtration (Yamada and Seki 2005), inertial movement (Di Carlo 2009), and hydraulic driving (Kim et al. 2015), take advantages of simple instruments and relatively high throughput.

Among the above-mentioned manipulation techniques, the theoretical and experimental researches on micro-particle or bio-organism manipulation assisted by acoustofluidic field, mainly including acoustic radiation forces and acoustic streaming induced drag forces, have gained rapid development and widespread attention (Lin et al. 2012; Hu 2014). Acoustic radiation forces originate from the interaction of sound fields with particles when there are acoustic property differences between particles and surrounding media (Bruus 2012a), while acoustic streaming vortices are usually caused by ultrasonic energy absorption in viscous media (Lighthill 1978a). Different from acoustic radiation force, acoustic streaming is a kind of steady fluidic flow and can be generated without the existence of particles in an acoustofluidic field (Friend and Yeo 2011). Acoustic manipulation methods are commonly considered to have inherent merits like low power consumption, little physiological harm to controlled bio-organisms (biocompatibility) (Wiklund 2012), contactless and non-invasive manipulation process (Lam et al. 2016), non-dependence on electromagnetic or optical properties (Connacher et al. 2018), and easy-to-use microfluidic devices (Ahmed et al. 2016), etc. At present, almost all of the ultrasonic manipulation methods depend on Gaussian beams (Mitri 2015), travelling/standing acoustic waves (Destgeer and Sung 2015), and special sound beams like vortex- or Bessel-beams (Wang et al. 2016a; Jiang et al. 2017), which are commonly generated by Langevin oscillators, piezoelectric buzzers, and interdigital transducers. However, further development and application of acoustic methods is obviously limited in the frequency range and output power provided by ultrasonic transducers and the diversity of sound field distributions, e.g., complex transducer arrays or obstacle arrangements are needed to satisfy the topological manipulation requirements of different kinds of micro/nano-particles and bio-organisms on lab-on-a-chip platforms. In recent years, diversity investigation of acoustofluidic fields has drawn more and more attention to achieve complicated distributions of acoustic radiation force and acoustic streaming for fascinating applications in instantaneous patterning, customized fabrication, tissue/organ engineering, and other biological areas of use (Lu et al. 2017; Hao et al. 2020; Tang et al. 2019). Therefore, it is necessary and urgent to obtain diversified and complicated sound field distributions with relatively simple ultrasonic oscillation devices.

Fortunately, with the theoretical researches and experimental verification of phononic crystals and acoustic metamaterials, it is possible now to make breakthroughs in terms of ultrasonic manipulations of various micro/nano-particles and bio-samples with the assistance of artificial metamaterials and metastructures (Hussein et al. 2014). Phononic crystal structures, which are made of periodic distributions of inclusions embedded in regular matrix arrangements, can provide a feasible way to reconstruct localized vibration modes with different sound field distributions (Dai et al. 2019a; Liu et al. 2000). Due to the periodic variations of acoustic quantities such as mass density and sound speed, these artificially engineered materials exhibit a series of band-pass and band-stop frequencies. The emerging interest in these artificial metamaterials streams from the possibility of achieving diverse acoustofluidic fields with relatively inexpensive equipments. For instance, precisely controlling sound wave propagation path results in highly-efficient acoustic lens (Kanno et al. 2013) and miraculous acoustic cloaking (Zheng et al. 2014). Also, different kinds of acoustic radiation forces and acoustic streaming fields modulated by phononic crystal structures have played increasingly important roles in the field of sound wave modulation, solution droplet movement, microfluidic mixing/nebulisation, particle/bio-organism manipulation and biomedical applications (Ke et al. 2006; Bourquin et al. 2010, 2011, 2016b, 2019,2020; Wilson et al. 2011; Cai et al. 2011; Reboud et al. 2012a, b; Qiu et al. 2014; Xu et al. 2014; Li et al. 2014, 2018a, b; c; Wang et al. 2015; Feng et al. 2015; Xia et al. 2017; Dai et al. 2019b; Hsu and Lin 2019).

To further investigate the formation mechanism of acoustofluidic field modulated by phononic crystal structures, we introduced C-shaped phononic crystal configurations, following the structural design of Elford et al. (2011), to generate different acoustofluidic patterns for micro-particle manipulation only by modulating the input frequency of incident acoustic wave. Particle trajectory under the influence of acoustic radiation force and acoustic streaming induced drag force is simulated to demonstrate the manipulation performance of massive micro-particles. Also, it is found that more types of acoustic streaming vortices can be generated under the modulation of defective or asymmetric phononic crystal plates. In general, our exploratory work combining plain slotted phononic crystal structures and acoustofluidics can offer flexibility to control acoustic streaming fields in microfluidic devices for various applications, which is expected to be a promising tool for the investigation of generation mechanism of acoustic streaming vortices, rapid microfluidic mixing of different media and

particles on a disposable chip, and non-contact manipulation and rotation of bio-samples for the following surface morphology observation and phenotype characterization (Tang et al. 2020).

2 Theory and simulation process

The fundamental governing equations of acoustofludic field generated by incident sound waves in a two-dimensional (2D) chamber have been studied extensively in the literatures (Bruus 2012b; Sadhal 2012; Lei et al. 2017). Here, we briefly introduce the perturbation theory and relevant simulation process for completeness. Sound energy emitted from the vibration sources into viscous medium and boundary layer is nonlinear. This effect can cause time-independent acoustic radiation force and steady fluid flow known as acoustic streaming in a microfluidic chamber (Wiklund et al. 2012). Here, the fluidic medium is assumed to be homogeneous and isotropic, in which the continuity and momentum equations for the fluid flow can be expressed as

$$\frac{\partial \rho}{\partial t} + \nabla \cdot (\rho \mathbf{u}) = 0, \tag{1}$$

$$\rho\left(\frac{\partial \mathbf{u}}{\partial t} + \mathbf{u} \cdot \nabla \mathbf{u}\right) = -\nabla p + \mu \nabla^2 \mathbf{u} + \left(\mu_b + \frac{1}{3}\mu\right)\nabla\nabla \cdot \mathbf{u}, \tag{2}$$

where ρ is the fluid density, t is time, $\mathbf{u}$ is the fluid velocity vector, p is the pressure, and μ and μ_b are the dynamic and bulk viscosity coefficients of the fluid, respectively. The left-hand side of Eq. (2) represents the inertial force per unit volume on the fluid with the two terms in the bracket being the unsteady acceleration and convective acceleration of a fluid volume element, respectively. The right-hand side indicates the divergence of stress, including the pressure gradient and the viscosity forces. Other forces, such as gravity force and buoyancy force, are not considered, because they are generally negligible compared to the above-mentioned driving forces (Lei et al. 2018). In the case of small oscillation amplitude, the induced fluidic response can be expressed using a perturbation expansion, and the fluid density, pressure, and velocity are written as

$$\rho = \rho_0 + \rho_1 + \rho_2 + \cdots, \tag{3}$$

$$p = p_0 + p_1 + p_2 + \cdots, \tag{4}$$

$$\mathbf{u} = \mathbf{u}_1 + \mathbf{u}_2 + \cdots, \tag{5}$$

where the subscripts 0, 1, and 2 represent the static (absence of sound), first-order, and second-order quantities, respectively. The unwritten higher order terms in Eqs. (3)–(5) can be ignored in the following calculation of first-order sound field and second-order acoustic streaming field because of higher order infinitesimal quantities (Bruus 2012b). Substituting Eqs. (3)–(5) into Eqs. (1) and (2) and considering the first-order terms can yield

$$\frac{\partial \rho_1}{\partial t} + \rho_0 \nabla \cdot \mathbf{u}_1 = 0, \tag{6}$$

$$\rho_0 \frac{\partial \mathbf{u}_1}{\partial t} = -\nabla p_1 + \mu \nabla^2 \mathbf{u}_1 + \left(\mu_b + \frac{1}{3}\mu\right)\nabla\nabla \cdot \mathbf{u}_1. \tag{7}$$

Repeating the above procedure for the second-order terms, followed by time averaging over a period of oscillation, yields a second-order acoustic streaming field:

$$\overline{\frac{\partial \rho_2}{\partial t}} + \rho_0 \nabla \cdot \overline{\mathbf{u}_2} + \nabla \cdot \overline{\rho_1 \mathbf{u}_1} = 0, \tag{8}$$

$$\rho_0 \overline{\frac{\partial \mathbf{u}_2}{\partial t}} + \rho_1 \overline{\frac{\partial \mathbf{u}_1}{\partial t}} + \rho_0 \overline{\mathbf{u}_1 \cdot \nabla \mathbf{u}_1} = -\nabla \overline{p_2} + \mu \nabla^2 \overline{\mathbf{u}_2} + \left(\mu_b + \frac{1}{3}\mu\right)\nabla\nabla \cdot \overline{\mathbf{u}_2}, \tag{9}$$

where the upper bar represents a time-averaged value over a full oscillation time period. For the steady second-order acoustic streaming field, $\frac{\partial \rho_2}{\partial t} = 0$ and $\frac{\partial \mathbf{u}_2}{\partial t} = 0$, thus Eqs. (8) and (9) can be simplified as

$$\rho_0 \nabla \cdot \overline{\mathbf{u}_2} = -\nabla \cdot \overline{\rho_1 \mathbf{u}_1}, \tag{10}$$

$$\nabla \overline{p_2} - \mu \nabla^2 \overline{\mathbf{u}_2} - \left(\mu_b + \frac{1}{3}\mu\right)\nabla\nabla \cdot \overline{\mathbf{u}_2} = -\left(\rho_0 \overline{\mathbf{u}_1 \cdot \nabla \mathbf{u}_1} + \overline{\rho_1 \frac{\partial \mathbf{u}_1}{\partial t}}\right), \tag{11}$$

where $\overline{\mathbf{u}_2} = \mathbf{u}_2$ and $\overline{p_2} = p_2$ are the time-independent acoustic streaming velocity and pressure needed to be calculated, respectively. Thus, Eqs. (10) and (11) can also be written as

$$\rho_0 \nabla \cdot \mathbf{u}_2 = -\nabla \cdot \overline{\rho_1 \mathbf{u}_1}, \tag{12}$$

$$\nabla p_2 - \mu \nabla^2 \mathbf{u}_2 - \left(\mu_b + \frac{1}{3}\mu\right)\nabla\nabla \cdot \mathbf{u}_2 = -\left(\rho_0 \overline{\mathbf{u}_1 \cdot \nabla \mathbf{u}_1} + \overline{\rho_1 \frac{\partial \mathbf{u}_1}{\partial t}}\right). \tag{13}$$

Combining Eqs. (6, 7, 12, and 13) with appropriate boundary conditions, sound field and acoustic streaming field produced by incident acoustic waves combing different phononic crystal plates can be numerically solved using the commercial finite element software COMSOL Multiphysics (version 5.5, COMSOL AB, Stockholm, Sweden). The computational process consists of the following three steps.

In the first step, the first-order acoustic pressures and velocity fields produced by incident acoustic waves at different frequency points are calculated by the 'Thermoviscous

Acoustics, Frequency Domain' module in the COMSOL Multiphysics using frequency sweeping function. Initial settings and boundary conditions of the sound fields are as follows: the background sound pressures and frequencies of incident acoustic waves are set by users; the rest of the acoustic boundaries are set to be isothermal and slip. Equations (6) and (7) are used in the calculation of first-order sound fields modulated by phononic crystal plates.

In the second step, computed vibration velocity and pressure of the sound field at each frequency point are used to calculate the mass source term $-\nabla \cdot \overline{\rho_1 \mathbf{u}_1}$ of Eq. (12) and the volume force term $-\left(\rho_0 \overline{\mathbf{u}_1 \cdot \nabla \mathbf{u}_1} + \rho_1 \overline{\frac{\partial \mathbf{u}_1}{\partial t}}\right)$ of Eq. (13), respectively, by the post-processing functions of COMSOL Multiphysics, which act as the driving force of acoustic streaming field in an acoustofluidic chamber.

In the last step, the steady acoustic streaming is solved by the fluidic dynamics module 'Laminar Flow' of COMSOL Multiphysics, and the inertial term (Stokes flow) of fluid flow can be neglected, for the reason that the inertial force $\rho_0(\mathbf{u}_2 \cdot \nabla)\mathbf{u}_2$ is usually negligible compared with the mass source term and the volume force term in a low-speed acoustic streaming field (Lei et al. 2017). Equations (12) and (13) are used in the calculation of acoustic streaming, and all of the fluidic boundaries are set to be non-slip boundary condition. To ensure the convergence of the computational results, weak contributions of mass source and acoustic streaming pressure are added in the fluidic dynamics module (Muller et al. 2012).

On the basis of simulated ultrasound field and acoustic streaming field, a COMSOL 'Particle Tracing for Fluid' interface can be added to compute the motion of microparticles in a background flow field. Particle motion in the microfluidic chamber is driven by acoustic radiation force $\mathbf{F}_{\mathrm{rad}}$ (acoustophoretic force) and Stokesian drag force $\mathbf{F}_{\mathrm{drag}}$ (Karlsen and Bruus 2015; Tang et al. 2017, 2018), which can be expressed as

$$\mathbf{F}_{\mathrm{rad}} = -\frac{4}{3}\pi R_{\mathrm{p}}^3 \nabla \left[\frac{1-\beta}{2\rho_0 c_0^2} \overline{p_1^2} - \frac{D}{2}\rho_0 \overline{\|\mathbf{u}_1\|^2} \right], \tag{14}$$

$$\mathbf{F}_{\mathrm{drag}} = 6\pi\mu R_{\mathrm{p}}(\mathbf{u}_2 - \mathbf{u}_{\mathrm{p}}), \tag{15}$$

where R_{p} and $\mathbf{u}_{\mathrm{p}}$ are the spherical particle radius and velocity, respectively. The parameters β and D are defined as

$$\beta = \frac{\rho_0 c_0^2}{\rho_{\mathrm{p}} c_{\mathrm{p}}^2}, \tag{16}$$

$$D = \frac{3(\rho_{\mathrm{p}} - \rho_0)}{2\rho_{\mathrm{p}} + \rho_0}, \tag{17}$$

where ρ_{p} and c_{p} are the density and sound speed of spherical particles, respectively. From the acoustic radiation force and streaming-induced drag force that have been calculated, neglecting the buoyancy force and gravity force of microparticles in an acoustofluidic chamber, particle trajectories can be simulated, following Newton's second law of motion (Lei 2017)

$$\frac{\mathrm{d}}{\mathrm{d}t}\left(\rho_{\mathrm{p}}\frac{4}{3}\pi R_{\mathrm{p}}^3 \mathbf{u}_{\mathrm{p}}\right) = \mathbf{F}_{\mathrm{rad}} + \mathbf{F}_{\mathrm{drag}}. \tag{18}$$

In addition to the above-mentioned main driving forces ($\mathbf{F}_{\mathrm{rad}}$ and $\mathbf{F}_{\mathrm{drag}}$), the particle–particle interaction force is also considered in the particle trajectory simulation process to avoid neighboring particles being concentrated to a single point. The particle–particle interaction force can be expressed as

$$\mathbf{F}_{\mathrm{p-p}} = -k_s \sum_{j=1}^{N} \left(\left|\mathbf{r} - \mathbf{r}_j\right| - r_0\right) \frac{\mathbf{r} - \mathbf{r}_j}{\left|\mathbf{r} - \mathbf{r}_j\right|}, \tag{19}$$

where k_s is the spring constant, $\mathbf{r}_j$ is the position vector of the jth particle, and r_0 is the equilibrium position between particles, which is defined as $2R_{\mathrm{p}}$ (Lei et al. 2017). The wall condition of all boundaries is typically set as bounce when tracing micro-scale particles in a fluid field.

The simulation model of the 2D microfluidic chamber utilized to calculate the acoustofluidic field behind a configured phononic crystal plate is shown in Fig. 1a. The whole microfluidic chip is composed of five regions, among which region 1 and region 5 are set to be perfectly matched layers (PML), absorbing all acoustic energy in all frequency ranges without any impedance mismatch causing spurious reflections; Region 2 is set to be the background acoustic field with incident plane wave along the positive propagation direction of x-axis; region 3 contains the phononic crystal plate, comprising C-shaped slotted rings with inner radius 50 μm, external radius 65 μm and slot width 20 μm which are arranged in a 5×10 array in water; region 4 is where the transmitted acoustic wave is modulated by the phononic crystal plate and the acoustic streaming field needs to be calculated. All of the structural parameters are annotated in Fig. 1a and Table 1 without more description. Figure 1b shows a meshed model of the acoustofluidic chamber with locally magnified views of mapped quadrilateral mesh condition in regions 1, 2, 4, and 5 and free triangular mesh condition in region 3. The maximum element size of all grids is set to be 5 μm, which is 10% of the ultrasonic wavelength at the predefined maximum frequency point of 30 MHz $\left(\lambda = \frac{c_0}{f} = \frac{1500\ \mathrm{m}}{30\ \mathrm{MHz}} = 50\ \mu\mathrm{m}\right)$ (Bruus 2012b). The total number of grid cells in the simulation is about 455,250. The detailed boundary conditions of the sound field and acoustic streaming calculation in the 2D acoustofluidic

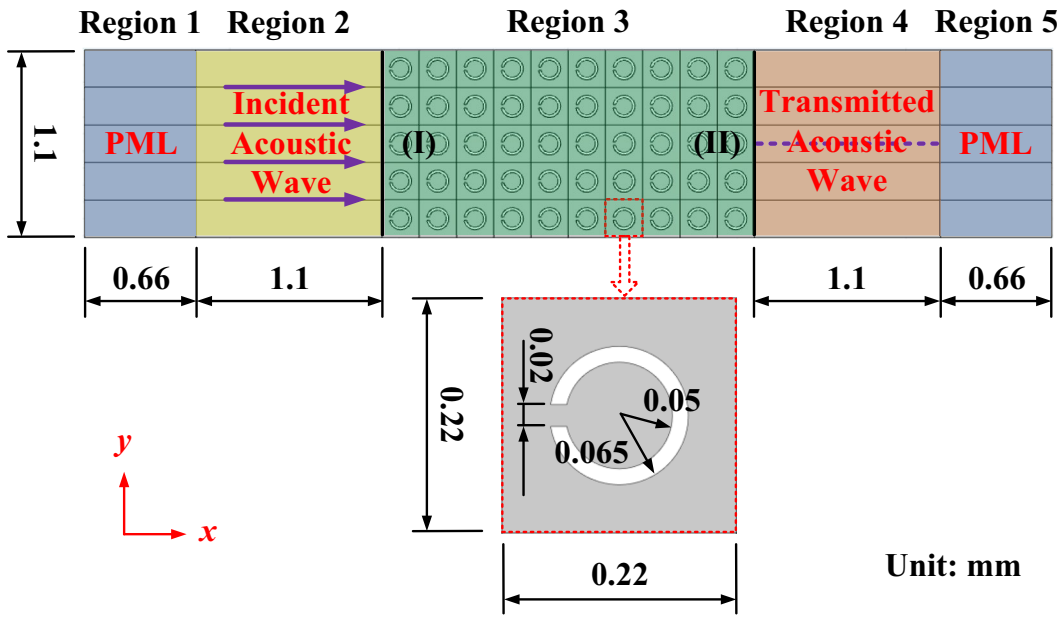

(a)

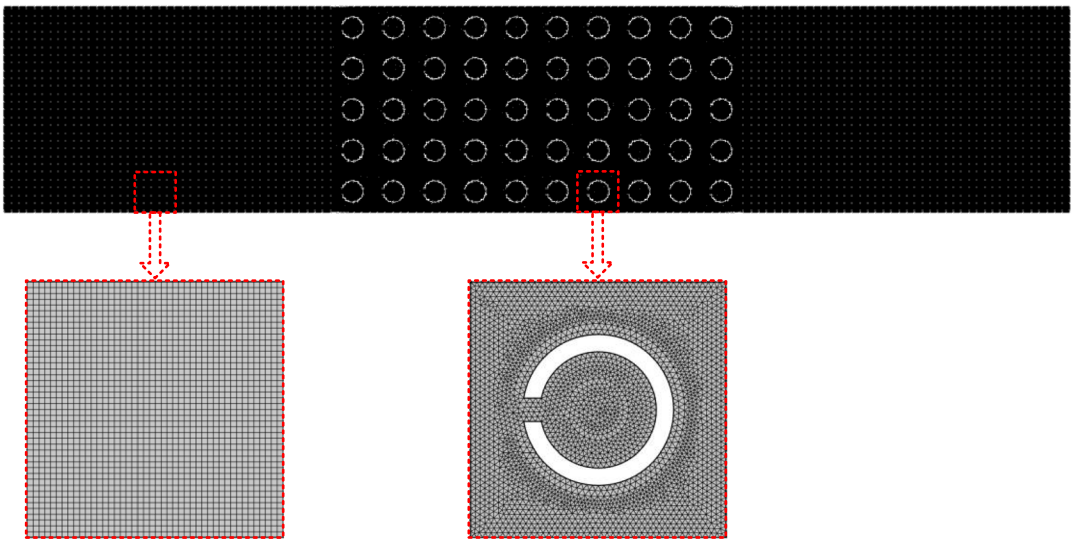

(b)

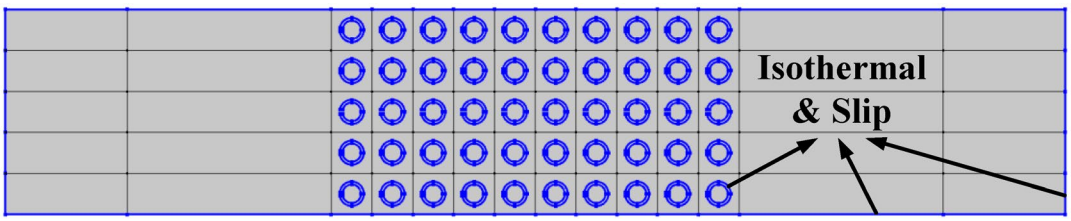

(c)

Fig. 1 2D model for the acoustofluidic field simulation modulated by phononic crystal plate with C-shaped slotted rings. **a** Computational model. **b** Meshed model. **c** Boundary condition of sound field. **d** Boundary condition of acoustic streaming field. **e** Simulated sound pressure along the purple dotted line under different grid scales

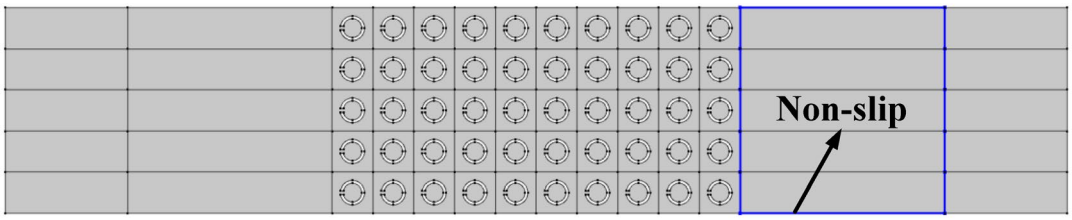

(d)

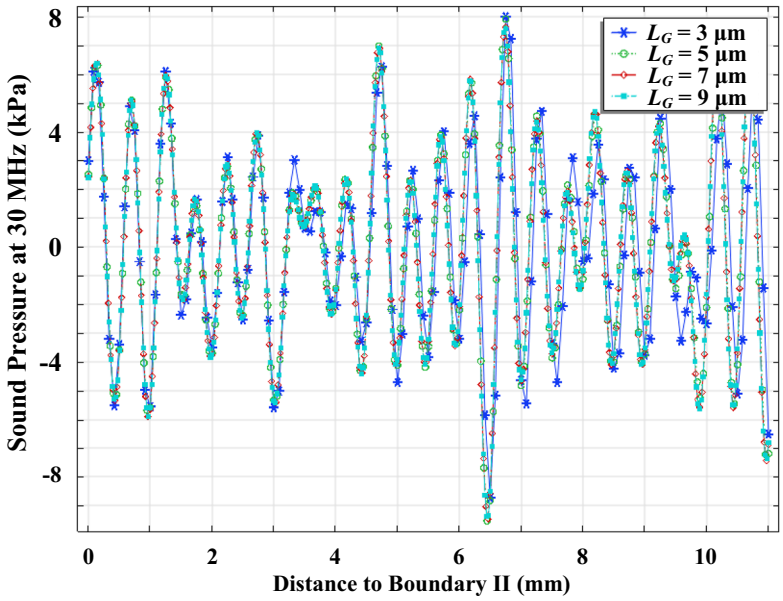

(e)

Fig. 1 (continued)

chamber are shown in Fig. 1c, d, respectively. The simulation time of sound field sweeping from 1 to 30 MHz with a step value of 0.1 MHz takes several hours, and the total simulation time of acoustic streaming field and movement trajectory of 10,000 micro-particles (polystyrene beads) at each selected frequency point only takes several minutes, using a DELL T5820 Tower workstation with a 128 GB memory (Dell Inc., Shanghai Subsidiary, Shanghai, China).

To prove that all the simulation results are convergent and mesh-independent, the maximum frequency point (30 MHz) in the our simulation is chosen as a reference point to calculate the sound field distribution along the purple dotted line (see Fig. 1a) under different grid scales, and the simulated sound pressure curves are plotted in Fig. 1e. It is found that the data variation among the maximum sound pressures under different mesh sizes is less than 5%. Therefore, it can be concluded that all the calculation results of sound field and acoustic streaming distribution are mesh-independent when the maximum element size of all grids is set to be 5 μm as the grid subdivision standard throughout our simulation. Unless otherwise specified, the model parameters including structural design, oscillation setting, and medium properties in the simulation are all listed in Table 1.

3 Simulation results and discussion

By solving for a parametric sweeping of input frequency, a frequency spectrum displaying the transmission properties of the phononic crystal structure can be constructed to show attenuation peaks and assist in finding the available frequency points of sharply defined acoustic streaming field. A comparison of the transmission loss spectrum from 1 to 30 MHz against the computed band structure, limited to the ΓX direction, is shown in Fig. 2. The transmission loss level is defined as (Elford et al. 2011; Lighthill 1978b)

$$\mathrm{TL} = 10\log_{10}\frac{\mathrm{PW}_{\mathrm{out}}}{\mathrm{PW}_{\mathrm{in}}}, \tag{20}$$

Table 1 Model parameters in the simulation

Quantity	Abbreviation	Value	Unit
Length of PML	L_{PML}	1.1	mm
Width of PML	W_{PML}	0.66	mm
Side length of regions 2 and 4	L	1.1	mm
Side length of phononic crystal lattice	L_{PC}	0.22	mm
Inner radius of C-shaped rings	R_I	0.05	mm
Outer radius of C-shaped rings	R_O	0.065	mm
Slot width of C-shaped rings	W_S	0.02	mm
Background acoustic pressure of region 2	P_{B}	0.1	MPa
Input vibration frequency	f	Range (1, 0.1, 30)	MHz
Maximum element size of all grids	L_{G}	5	μm
Density of water	ρ_0	1000	kg/m^3
Speed of sound in water	c_0	1500	m/s
Shear viscosity of water	μ	0.001	Pa s
Volume-to-shear viscosity ratio in water	μ_{B}/μ	2.79	1
Heat capacity at constant pressure of water	C_P	4200	J/(kg·K)
Heat conductivity coefficient of water	k	0.6	W/(m·K)
Density of polystyrene bead	ρ_{p}	1050	kg/m^3
Speed of sound in polystyrene bead	c_{p}	2400	m/s
Diameter of polystyrene bead	D_{p}	1	μm
Spring constant of polystyrene bead	k_s	2.5×10^{-4}	N/m

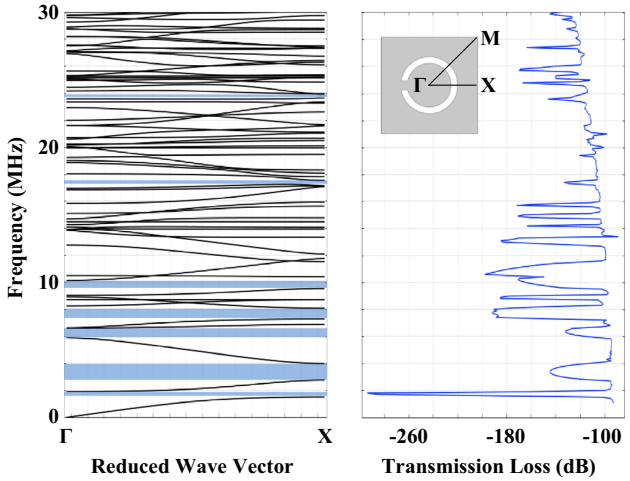

Fig. 2 A comparison of finite element computed band structure in the ΓX direction against the finite element computed frequency spectrum of transmission loss for C-shaped slotted rings

where $\mathrm{PW}_{\mathrm{in}}$ represents the incident power of plane wave and can be expressed as

$$\mathrm{PW}_{\mathrm{in}} = \int_{\text{boundary (I)}} \frac{P_B^2}{2\rho_0 c_0} \mathrm{d}L, \tag{21}$$

and $\mathrm{PW}_{\mathrm{out}}$ represents the transmitted power of acoustic wave modulated by the phononic crystal plate and can be expressed as

$$\mathrm{PW}_{\mathrm{out}} = \int_{\text{boundary (II)}} I \mathrm{d}L. \tag{22}$$

The integration boundaries (I) and (II) represented by black solid lines are shown in Fig. 1a. The sound intensity I can be written as

$$I = \frac{\|p_1\|^2}{2\rho_0 c_0}. \tag{23}$$

The frequency spectrum of transmission loss in Fig. 2 gives band gaps of larger width than those predicted by the finite element computed band structure. This difference could be attributed to the finite number of lattice elements used in the transmission simulations and the subsequent diffraction effects around the edges of the phononic crystal structures. The frequencies at which the band gaps occur in the band structure are in good agreement with the regions of attenuation peaks presented in the transmission spectrum.

With the assistance of band structure and transmission loss spectrum, we can preliminarily determine the frequency points that may generate sharply defined acoustic streaming field by choosing relatively lower attenuation points. According to Fig. 2, the frequency points with attenuation loss coefficients between − 100 and − 120 dB are mainly concentrated in the range from 10 to 30 MHz, which indicates that the frequency points which can be used in the acoustic streaming field generation are also concentrated

in the above-mentioned frequency range. By finite element calculation, it is obtained that the first frequency point that can produce sharply defined acoustic streaming vortices is located at 11.8 MHz, and the simulated acoustofluidic fields including sound pressure distribution, sound intensity pattern, and acoustic streaming field in region 4 are listed from Fig. 3a–c. Comparing the simulated acoustic streaming distribution with sound pressure and intensity patterns, it can be concluded that acoustic streaming field is determined by the sound intensity distribution rather than the sound pressure field, and acoustic streaming vortices flow out from the high-intensity areas and in from the low-intensity ones. Also by comparing Fig. 3a, c, it is found that approximately three wavelengths correspond to one vortex, where the wavelength

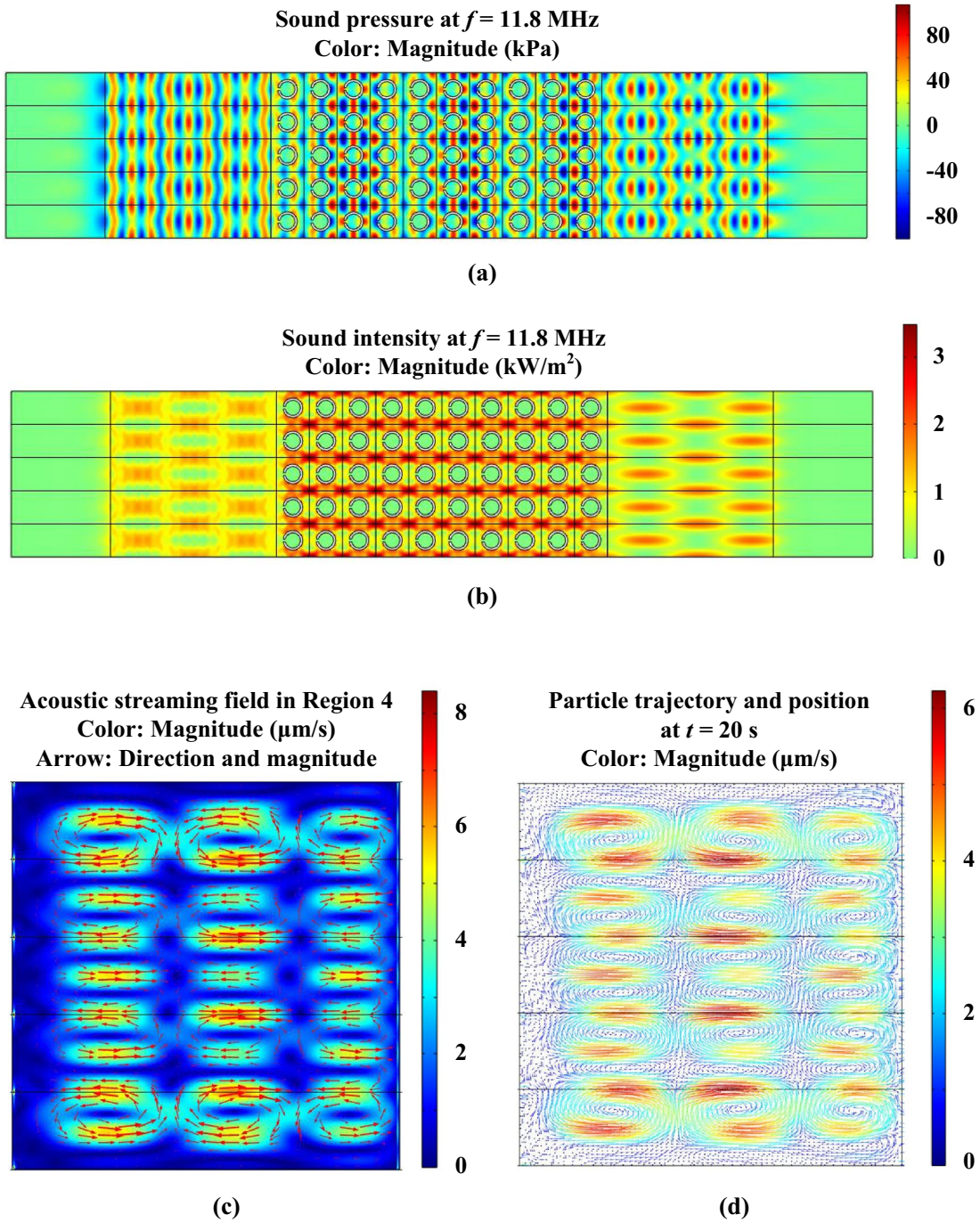

Fig. 3 Acoustofluidic fields and particle trajectory at 11.8 MHz. **a** Patterns of sound pressure. **b** Patterns of sound intensity. **c** Pattern of acoustic streaming field in region 4. **d** Patterns of particle trajectory at 20 s

refers to the distance between two neighbouring red peaks or blue troughs of sound pressure along the *x*-axis in region 4. Different from the staggered distribution of sound pressure or intensity field, such as the strong sound intensity areas represented by the red ellipses in Fig. 3b, the distribution of acoustic streaming vortices is arranged in an array form, and the neighbouring vortices flow in opposite directions. To ensure the calculation accuracy of particle trajectory in Fig. 3d, the acoustic streaming induced drag force and the acoustic radiation force are both considered in the simulation process of 1-μm-diameter particle movement at a given frequency point. However, compared with the streaming-induced drag force, the influence of acoustic radiation force can be neglected, and the simulated particle trajectory with comet tails is qualitatively consistent with the streamline of acoustic streaming field (Tang et al. 2019). The acoustofluidic fields modulated by the phononic crystal plate with C-shaped slotted rings are available for simultaneous rotation of massive micro-particles.

Additional eight working frequency points which can generate sharply defined acoustic streaming patterns are selected to further demonstrate the modulation function of phononic crystal structures on the acoustofluidic field only by switching the input frequency of background plane wave. With the increase of input frequency, the sound intensity patterns in regions 2 and 3 become more complicated, as shown in Fig. 4a. However, the sound intensity fields in region 4 modulated by the phononic crystal plate do not become disorganized as frequency increases, and the strong sound intensity areas are still arranged in array forms. The above conclusion can also be verified by the sound intensity distribution along the purple dotted line (see Fig. 1a) in region 4, as shown in Fig. 4b. The sound intensity curves along *x*-axis are quasi-periodic at different frequency points. Although waveform distortion becomes more noticeable at higher frequencies, obvious peaks and troughs of sound intensity can still be found in these curves. Based on the calculated sound intensity fields, acoustic streaming patterns in region 4 at different frequency points can be simulated, as shown in Fig. 4c. Due to the existence of phononic crystal plate, the increase of input frequency does not inevitably lead to complexity of acoustic streaming patterns, and the total number of vortices may even decrease at some certain frequency points, which is quite different from our previous conclusion that the distribution of acoustofluidic field in a 2D rectangular chamber becomes complicated with the increase of input frequency (Tang and Hu 2015). The velocity magnitude curves of acoustic streaming field along the purple dotted line (see Fig. 1a) at different input frequency points are also drawn in Fig. 4d to demonstrate the corresponding relationship between the sound intensity distribution and the acoustic streaming field. By comparing Fig. 4b, d, it can be obviously found that the waveforms and tendencies of the sound intensity and acoustic streaming velocity curves at the same frequency are similar except for data differences, which confirms the previous conclusion we have drawn from Fig. 3. However, a further comparison of Fig. 4b, reveals that acoustic streaming vortices produced by viscous attenuation of sound field can result in acoustic energy dissemination throughout the flow field. When the input frequency is 11.8 and 12.2 MHz, the maximum sound intensity is about 2 kW/m^2, while when the frequency is 15.4, 18.6 and 19.6 MHz, the maximum sound intensity is about 1.3 kW/m^2. However, at the above-mentioned frequency points, the maximum velocity magnitude values of the corresponding acoustic streaming fields are mainly around 6 μm/s. Even at 19.6 MHz, the acoustic streaming velocity only reaches a maximum value of 8 μm/s. The modulation results of acoustic streaming vortex numbers, locations and sizes at different frequency points assisted by phononic crystal structures may provide a novel perspective to manipulate numerous micro/nano-particles or bio-organisms and form organized patterns simultaneously at multiple given locations in a single microfluidic chamber.

On the basis of C-shaped slotted rings, another kind of phononic crystal plate with semicircular rings is introduced, as shown in Fig. 5a, together with the band structure and the transmission loss spectrum assisting in searching for the available frequency points of sharply defined acoustic streaming field. Compared with Fig. 2, the transmission loss curve in Fig. 5a has some minor changes in local tendency and attenuation peak points, which means that structural modification of phononic crystal lattices does have influences on sound field modulation. However, comparing the sound intensity field in Fig. 5b with the acoustic streaming patterns in Fig. 5d, the array-shaped distribution form of the acoustofluidic vortices has not essentially changed except that there are some deviations in the frequency points corresponding to the similar acoustic streaming vortex patterns, which means that the acoustic streaming field is relatively robust to the structural alteration of phononic crystal lattices. By comparing the distribution of sound intensity in Fig. 5c and acoustic streaming velocity in Fig. 5e along the purple dotted line (see Fig. 1a), a conclusion similar to that in Fig. 4 can be drawn, that is, the acoustic streaming vortices are determined by the sound intensity fields. More simulation results of acoustofluidic fields modulated by other kinds of phononic crystal plates are plotted in Figs. S1, S2 and S3 of the Supplementary Material.

If the C-shaped slotted rings are rotated by 90° clockwise, an phononic crystal plate asymmetric about the *x*-axis can be obtained, as shown in Fig. 6, together with the band structure in the ΓX direction and the frequency spectrum of transmission loss. Eight frequency points that can produce sharply defined acoustic streaming distribution are chosen to demonstrate the modulation function of asymmetric phononic

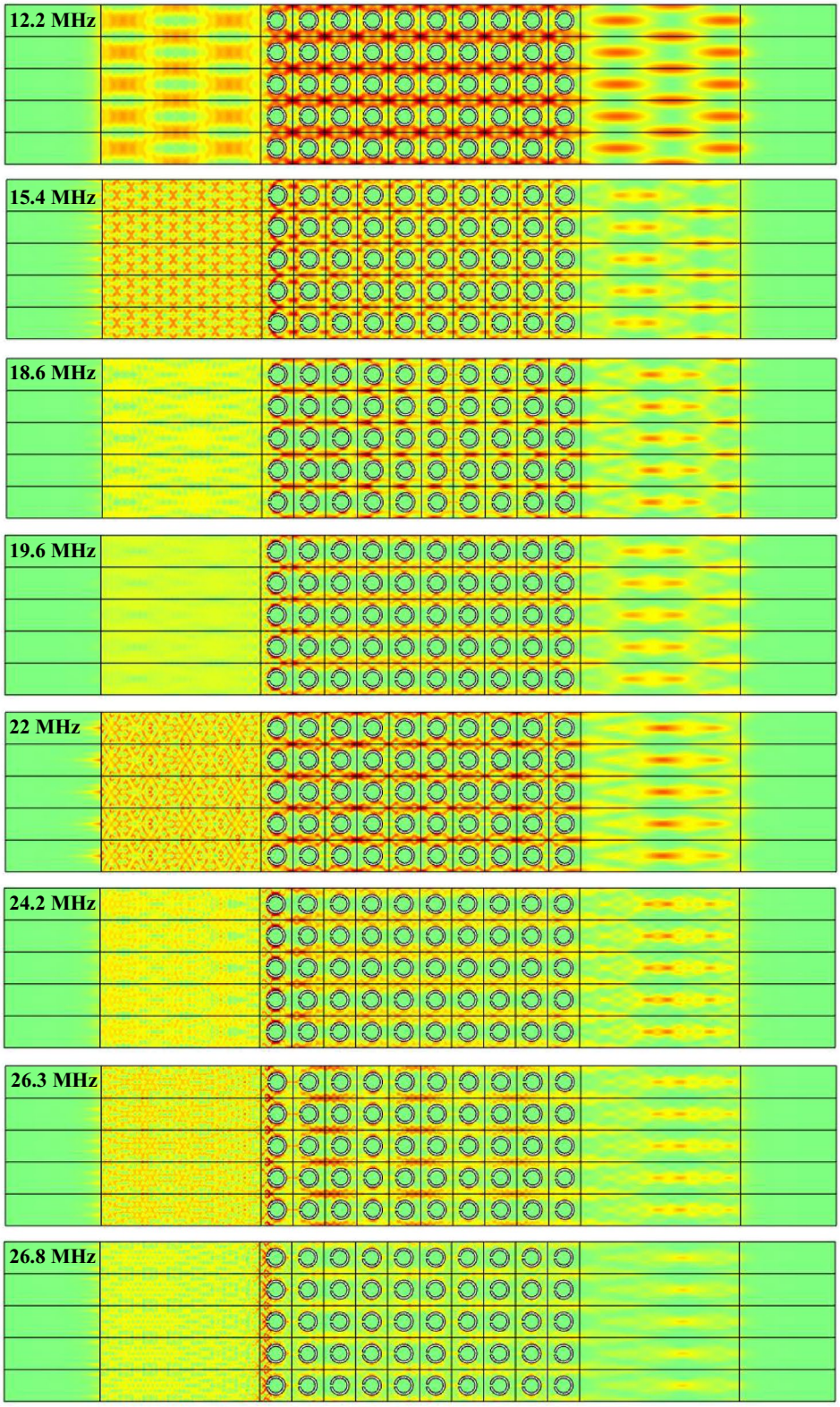

Fig. 4 Acoustofluidic fields generated by the phononic crystal plate with C-shaped slotted rings at different frequency points. **a** Patterns of sound intensity. **b** Sound intensity vs. distance to Boundary II. **c** Patterns of acoustic streaming field in region 4. **d** Acoustic streaming velocity magnitude vs. distance to Boundary II

Fig. 4 (continued)

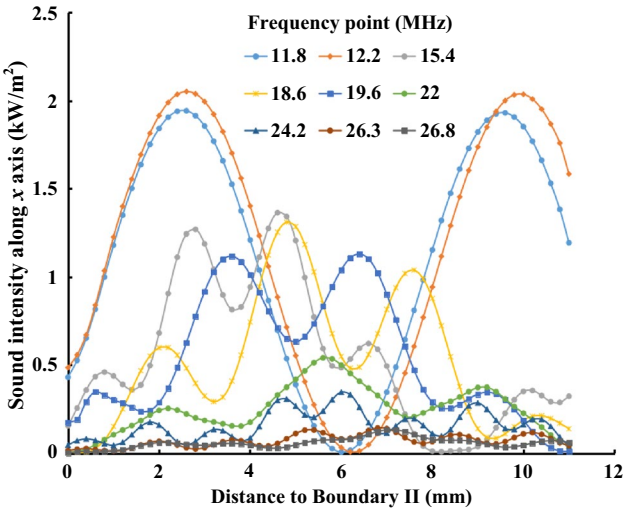

(b)

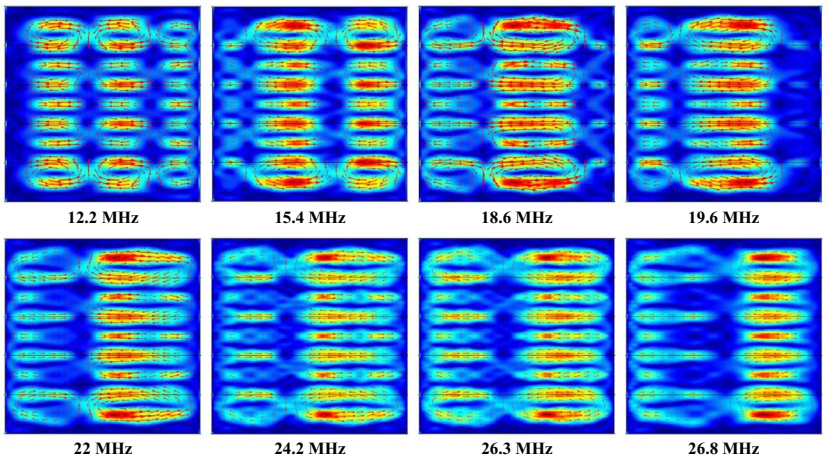

(c)

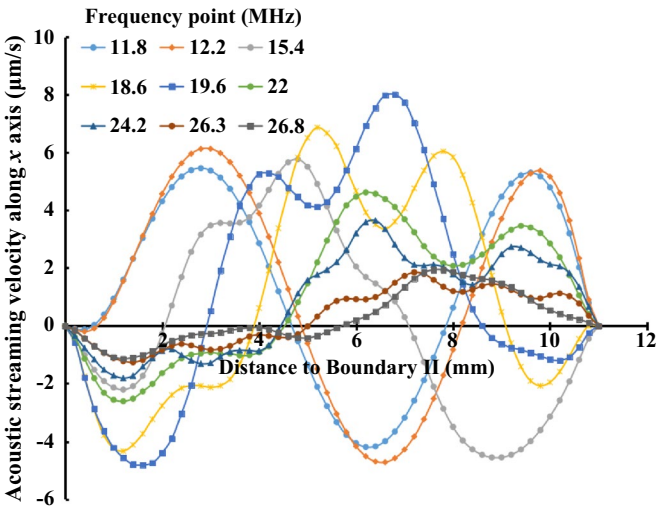

(d)

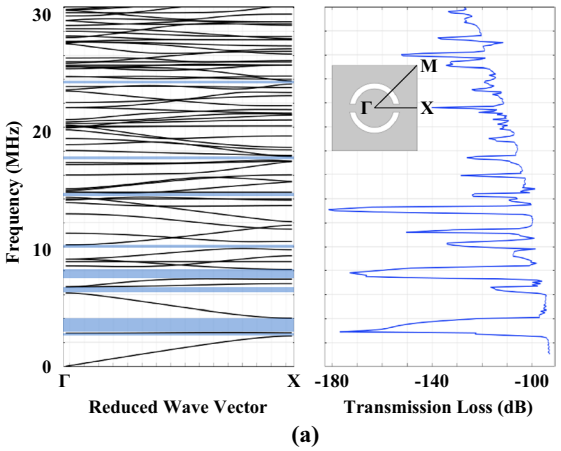

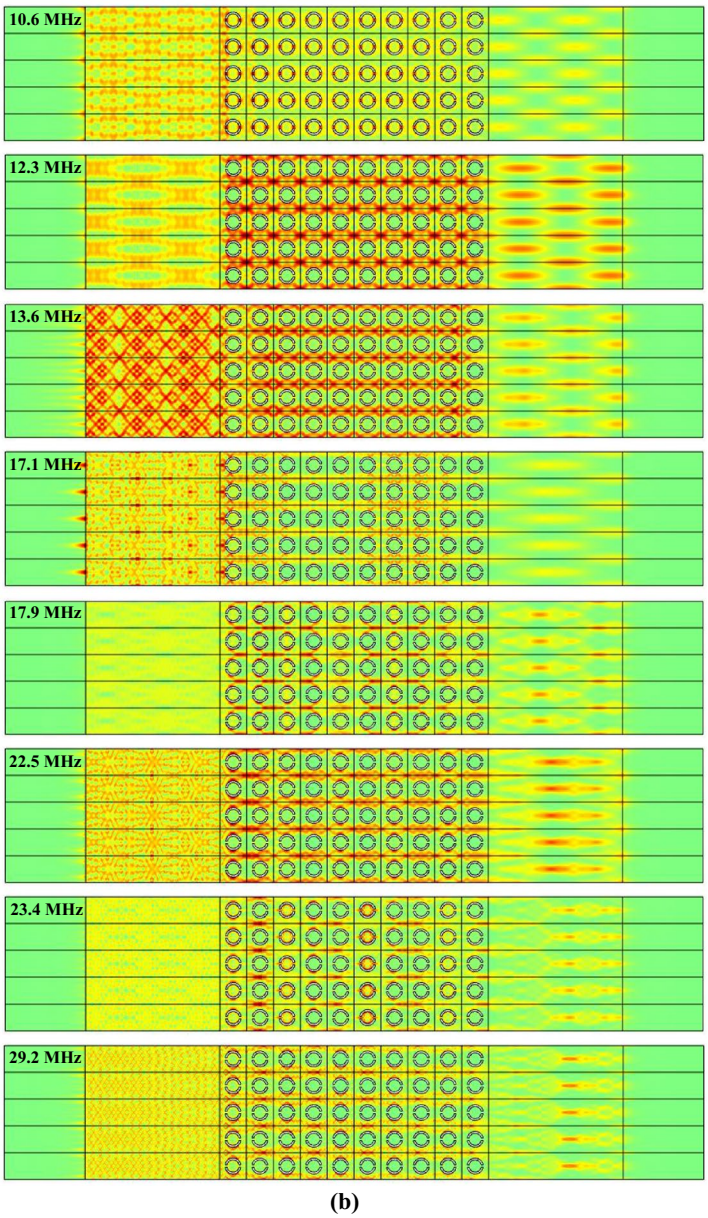

Fig. 5 Acoustofluidic fields generated by the phononic crystal plate with semicircular rings at different frequency points. **a** A comparison of band structure in the ΓX direction against the frequency spectrum of transmission loss. **b** Patterns of sound intensity. **c** Sound intensity vs. distance to Boundary II. **d** Patterns of acoustic streaming field in region 4. **e** Acoustic streaming velocity magnitude vs. distance to Boundary II

Fig. 5 (continued)

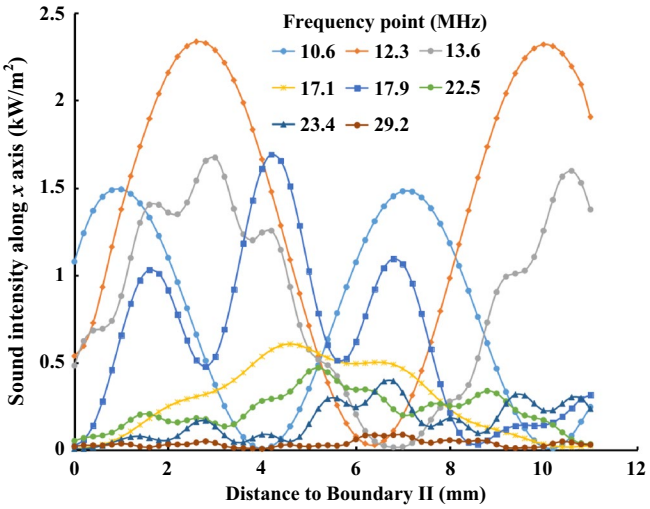

(c)

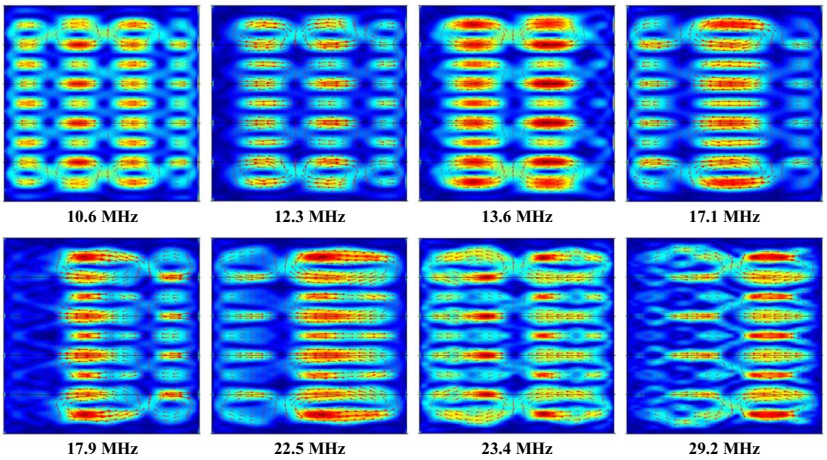

(d)

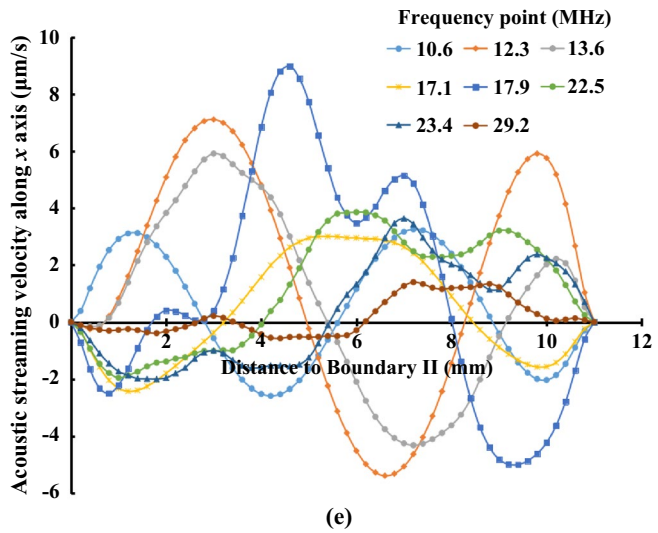

(e)

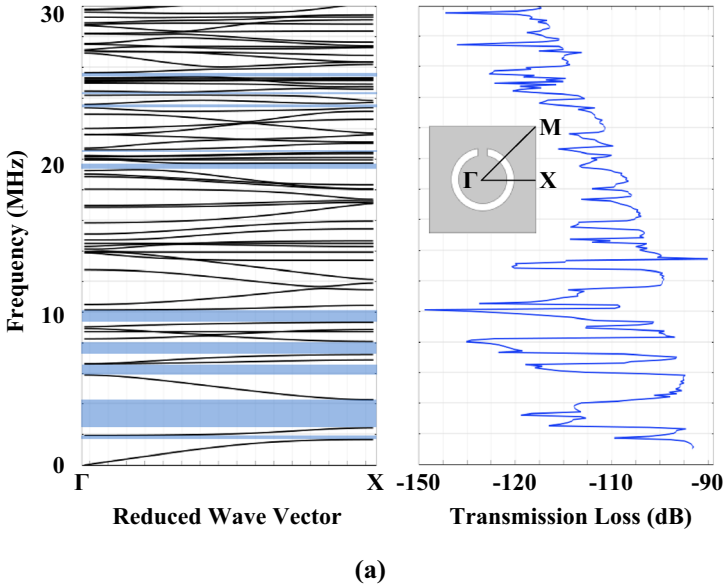

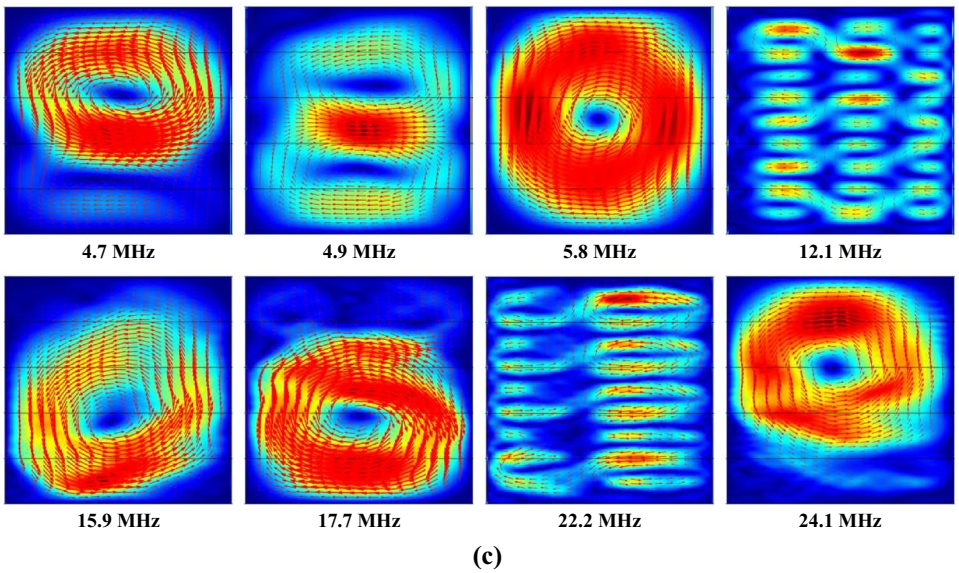

Fig. 6 Acoustofluidic fields generated by the phononic crystal plate with C-shaped slotted rings rotated by 90° clockwise at different frequency points. **a** A comparison of band structure in the ΓX direction against the frequency spectrum of transmission loss. **b** Patterns of sound intensity. **c** Patterns of acoustic streaming field in region 4

crystal structure on acoustofluidic field, and the corresponding sound intensity patterns and acoustic streaming vortices are shown in Fig. 6b, c, respectively. Due to the asymmetry of phononic crystal plate in the direction of sound propagation, the acoustic streaming fields obtained at most available frequency points consist of a single large vortex rotating clockwise or counterclockwise, such as 4.7, 5.8, 15.9, 17.7 and 24.1 MHz. Therefore, by switching the neighbouring frequency points back and forth, the orientation of acoustic streaming vortex in region 4 can be reversed constantly, which can be used to realize rapid mixing of micro-particles or bio-samples. By analyzing the sound intensity fields at the above-mentioned frequency points, it can be concluded that the large acoustic streaming vortices are generated when the strong sound intensity areas are mainly distributed on one side of region 4. However, at several certain frequency points, such as 4.9, 12.1 and 22.2 MHz, the distributions of sound intensity field and acoustic streaming vortices in region 4 are basically symmetric about the x-axis, as shown in Fig. 6b, c, respectively. Especially at the two frequency points of 12.1 and 22.2 MHz, the acoustic streaming vortices can form array arrangements, although there are minor distortions in the flow field distribution. Thus, acoustofluidic fields modulated by asymmetric phononic crystal plates can still be used for multipoint rotation and concentration of micro-particles at certain frequency points.

Inspired by lattice defect, a kind of defective phononic crystal plate is designed to modulate the sound field

Fig. 6 (continued)

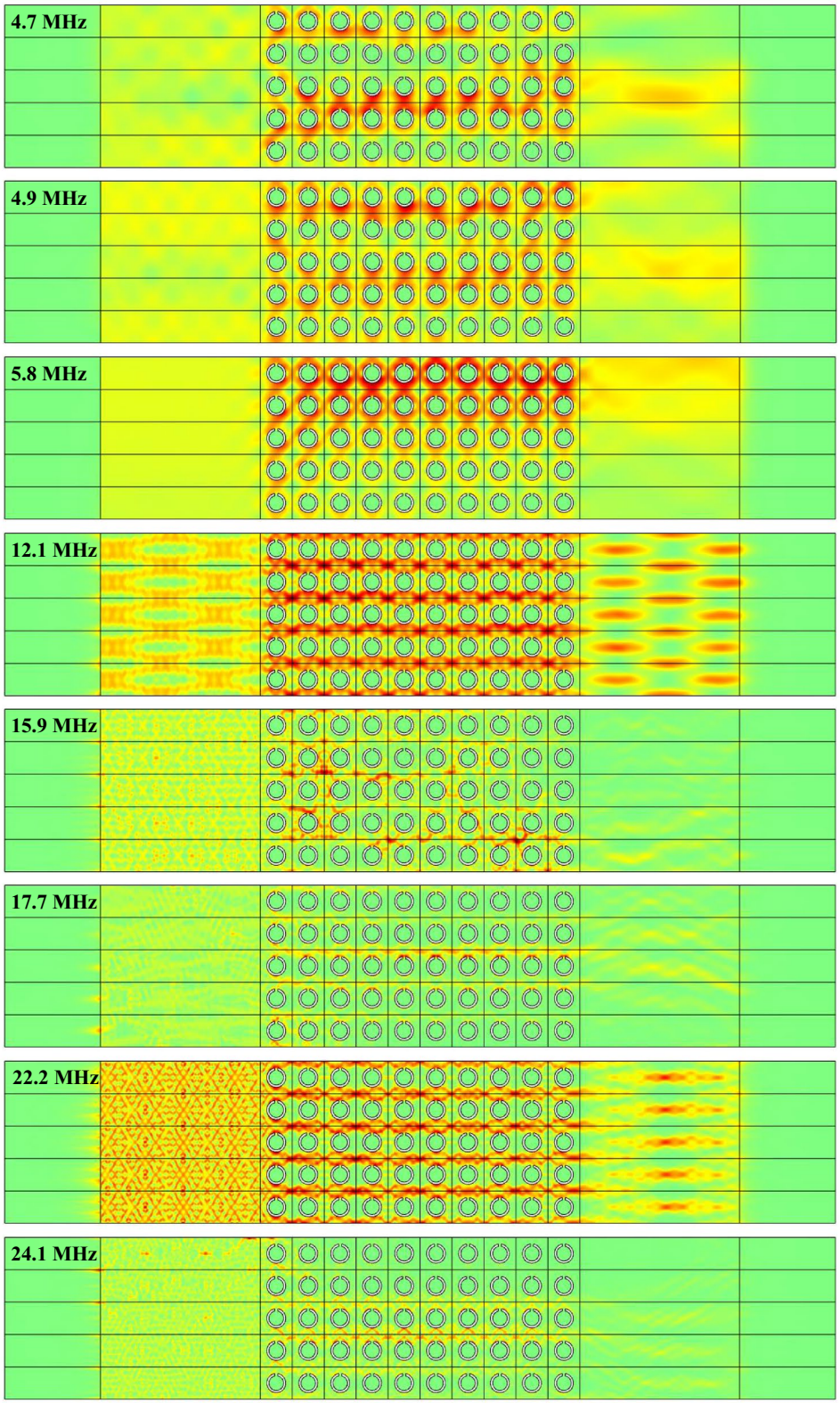

(b)

distribution and obtain more acoustic streaming patterns. As shown in Fig. 7a, the defective phononic crystal plate is obtained by removing the individual C-shaped ring element in the 3rd row and 1st column of the initial phononic crystal plate in region 3. Referring to the frequency spectrum of transmission loss obtained by the defective phononic crystal plate shown in Fig. 7a, eight frequency points which can form sharply defined acoustic streaming patterns are selected, and the sound intensity patterns corresponding to these frequency points are labeled in Fig. 7b. Due to structural defect of the phononic crystal plate, the sound intensity patterns in region 4 after modulation are no longer classic array arrangements. It can be found from the simulated acoustofluidic fields that acoustic streaming patterns generated at different frequency points from 4 to 11 MHz are mainly composed of two large vortices which are symmetric about the x-axis in region 4, and flow direction of these two large vortices varies repeatedly with the change of input frequency. As shown in Fig. 7c, at the frequency points of 4.1 and 5 MHz, the direction of the two large vortices flows out from the middle of the chamber and in from both sides, while at the frequency point of 4.4 MHz, the flow direction of the two large vortices changes and is opposite to the aforementioned one. By comparing the sound intensity patterns at the corresponding frequency points in Fig. 7b, the flow direction of the acoustic streaming vortices can be qualitatively explained, that is, the acoustic streaming vortices flow out from the high sound intensity areas and in from the low ones. The defective phononic crystal plate can guide the incident acoustic waves to propagate along different paths

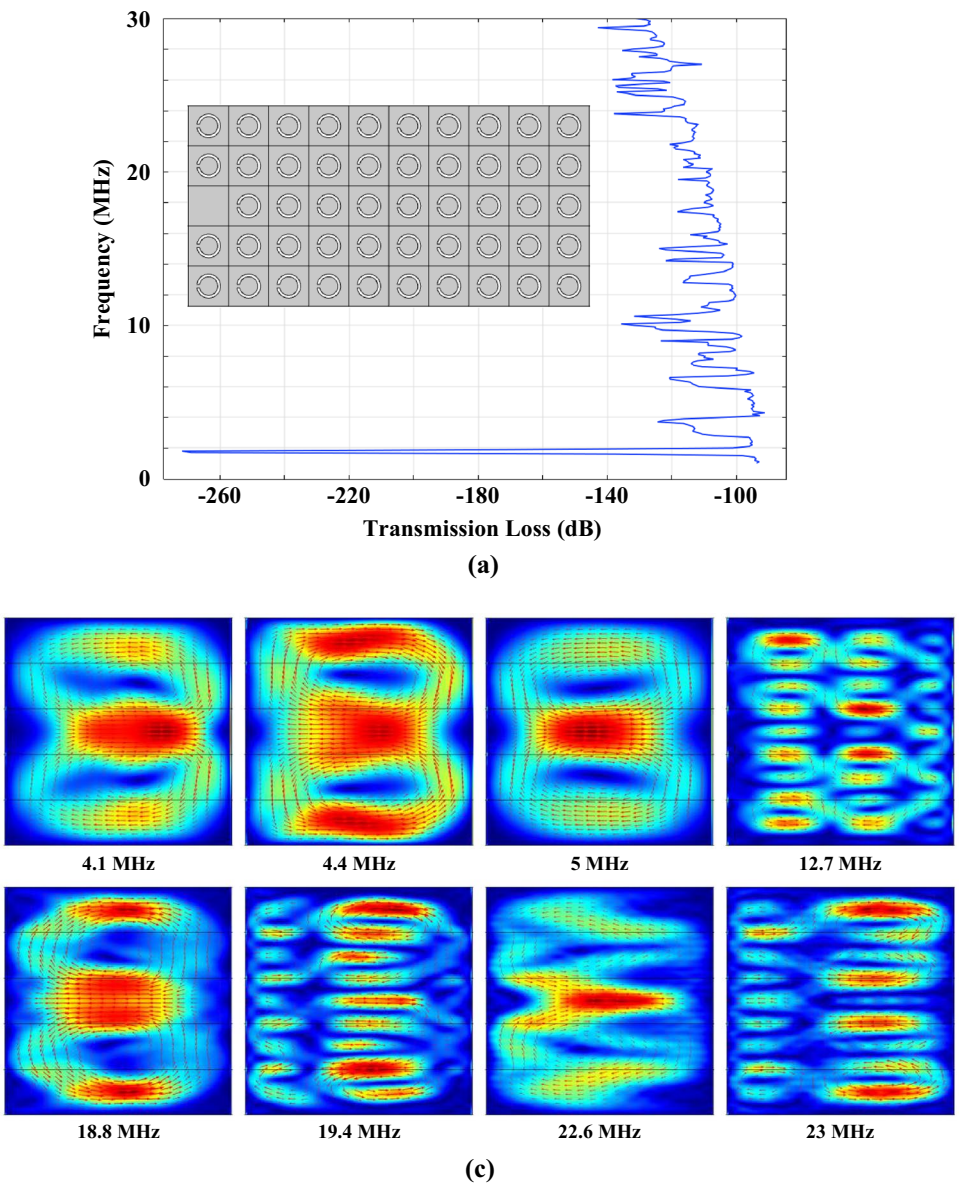

Fig. 7 Acoustofluidic fields generated by the defective phononic crystal plate obtained by removing the individual C-shaped ring element in the 3rd row and 1st column at different frequency points. **a** Frequency spectrum of transmission loss. **b** Patterns of sound intensity. **c** Patterns of acoustic streaming field in region 4

Fig. 7 (continued)

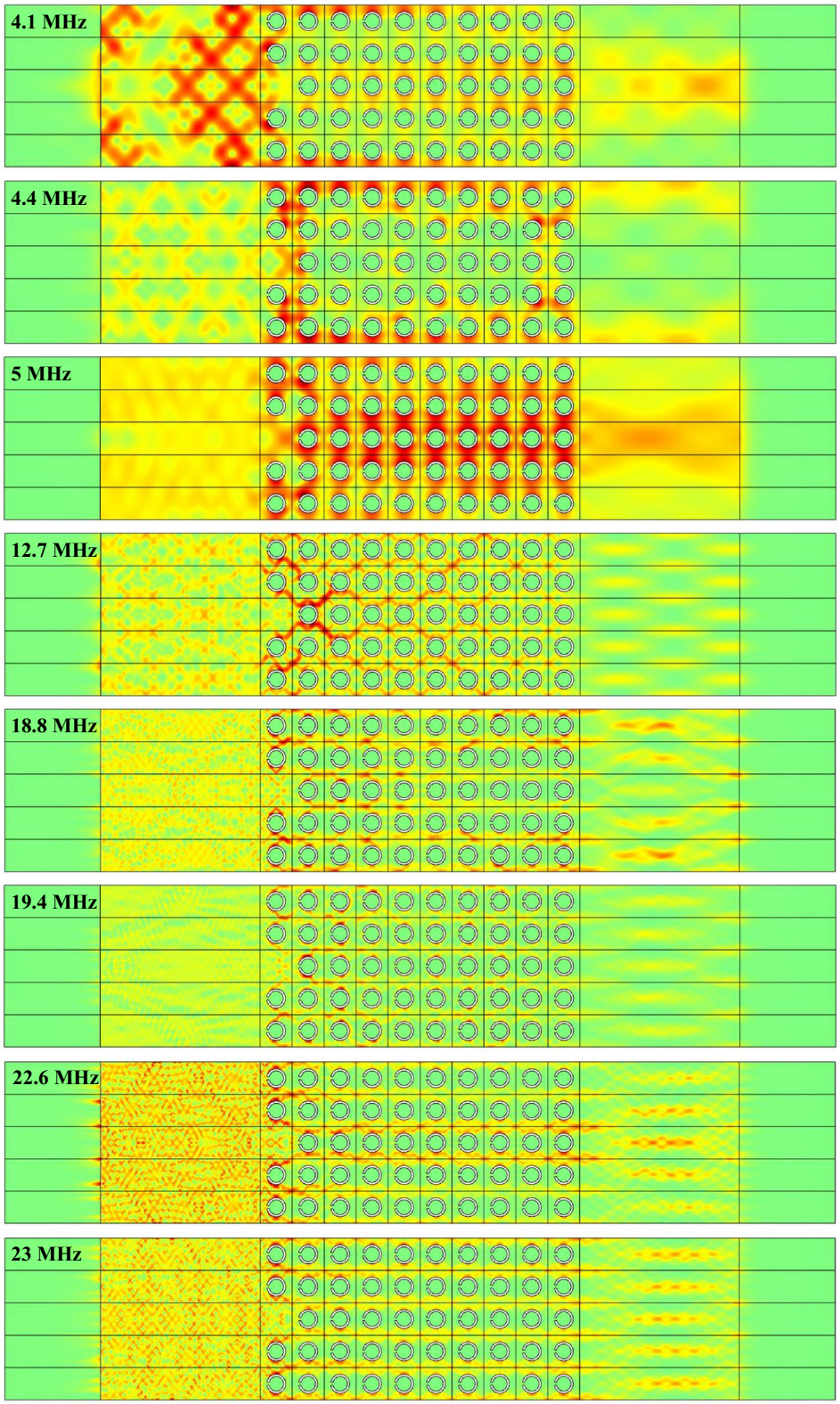

(b)

of the designed chamber at different frequency points, which can be applied for microfluidic mixing in the vicinity of several frequency points. Although large acoustic streaming vortices can also be generated at higher frequencies (18.8 and 22.6 MHz), the boundaries of these acoustic streaming patterns become ambiguous, together with vortex distortion and separation, as shown in Fig. 7c. Also, it is worth noting that slightly deformed array arrangement of acoustic streaming vortices can still be generated under the modulation of the defective phononic crystal plate at several input frequency points (12.7, 19.4 and 23 MHz), which can be explained by the sound intensity distribution of quasi-array arrangement in Fig. 7b.

As shown in Fig. 8, another kind of defective phononic crystal plate by removing the individual C-shaped ring element in the 3rd row and 6th column is designed. Compared with the frequency spectrum of transmission loss obtained from Fig. 7a, there are more attenuation peaks shown in Fig. 8a. Referring to the transmission loss diagram, six frequency points which can form sharply defined acoustic streaming patterns are selected. The sound intensity distributions and acoustic streaming patterns corresponding to these frequency points are labeled in Fig. 8b, c, respectively. Similar to the simulated acoustic streaming field in Fig. 7c, two large vortices which are symmetric about the *x*-axis can be generated in region 4, whose flow direction changes at different input frequency points (4.5 and 5.1 MHz in Fig. 8c). However, with the increase of input frequency (9.3, 11.8, and 12.6 MHz), large vortices break up into smaller ones, resulting in more complex and diverse patterns of acoustic streaming field, as shown in Fig. 8c. At the frequency point of 16.6 MHz, two large symmetric vortices can still be generated, while the vortex boundary becomes a little ambiguous. Different from the slightly deformed array arrangement of acoustic streaming vortices modulated by the defective phononic crystal plate in Fig. 7c, there is no possibility of generating similar acoustic streaming field when the defective element is located in the middle or end of the phononic crystal plate (see Fig. S4 in the Supplementary Material).

In summary, the simulation results of phononic crystal plates with different structures and arrangements provide the theoretical foundation and experimental protocols in the following researches combining phononic crystals/acoustic metamaterials with acoustofluidic fields. The modulation function of phononic crystal plates originates from the acoustic-structure coupling effects like reflection, scattering and diffraction along the sound propagation path. When manipulating bio-organisms or micro-/nano-scale objects, diverse acousotofluidic fields can be easily obtained only by changing the input frequency, waveform and number of the piezoelectric buzzers or interdigital transducers on existing microfluidic lab-on-a-chip platforms. In comparison with the previous work conducted by other research groups (Bourquin et al. 2010, 2011; Wilson et al. 2011; Reboud et al. 2012a, b), focused beams of ultrasound energy modulated by phononic crystal lattices provide a feasible scheme for liquid nebulisation/atomization and rapid rotation of biosamples in solution, while from our simulation results, it is found that array arrangement of acoustic streaming vortices can also be applied for simultaneous rotation and multipoint concentration of bio-organisms or micro-/nano-scale objects in an acoustofluidic chamber. Based on the above findings, it is feasible to introduce phononic crystal structures in the subsequent design and fabrication of microfluidic devices to generate diverse acoustic streaming vortices for a variety of novel applications, even if there are inevitable lattice defects of phononic crystal structures in the microfluidic chip manufacturing process due to inappropriate soft lithography and replica molding (Tang et al. 2020). This is because slightly deformed array arrangement of acoustic streaming vortices can still be generated through the frequency modulation of defective phononic crystal plates. The introduction of phononic crystals/acoustic metamaterials in microfluidic devices is innovative and fascinating, which will broaden the horizon in the applications of rapid mixing, simultaneous rotation and multipoint concentration of micro/nano-particles or bio-organisms on a disposable chip.

4 Conclusion

In this paper, a series of phononic crystal structure based acoustofluidic devices, which are actuated by incident plane waves at different frequency points, have been proposed and numerically investigated for microfluidic mixing and controllable manipulation of micro-/nano-scale particles. The introduction of phononic crystal structures can cause spatial variations of acoustofluidic field distribution along the sound propagation path, which is beneficial to overcome the monotonousness of acoustic streaming patterns in the existing lab-on-a-chip devices. Array arrangement of acoustic streaming vortices can be generated under the modulation of phononic crystal plates with C-shaped slotted or semicircular rings, and the vortex number, location and size can also be changed at different input frequency points. The movement trajectories of micro-particles under the combination of acoustic radiation forces and acoustic streaming induced drag forces are also simulated to demonstrate the particle manipulation performance of the phononic crystal structure based acoustofluidic devices. It is also verified that asymmetric or defective phononic crystal plates can be used to generate more types of acoustic streaming patterns. The introduction of different phononic crystal structures offers flexibility to modulate acoustofluidic fields in lab-on-a-chip devices for various applications. It is suggests the

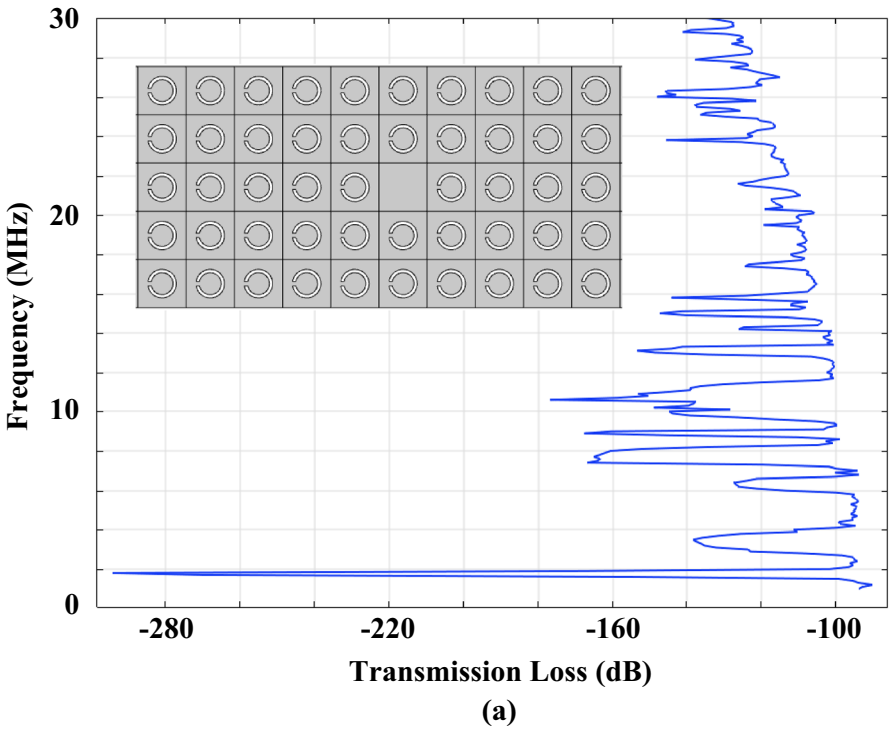

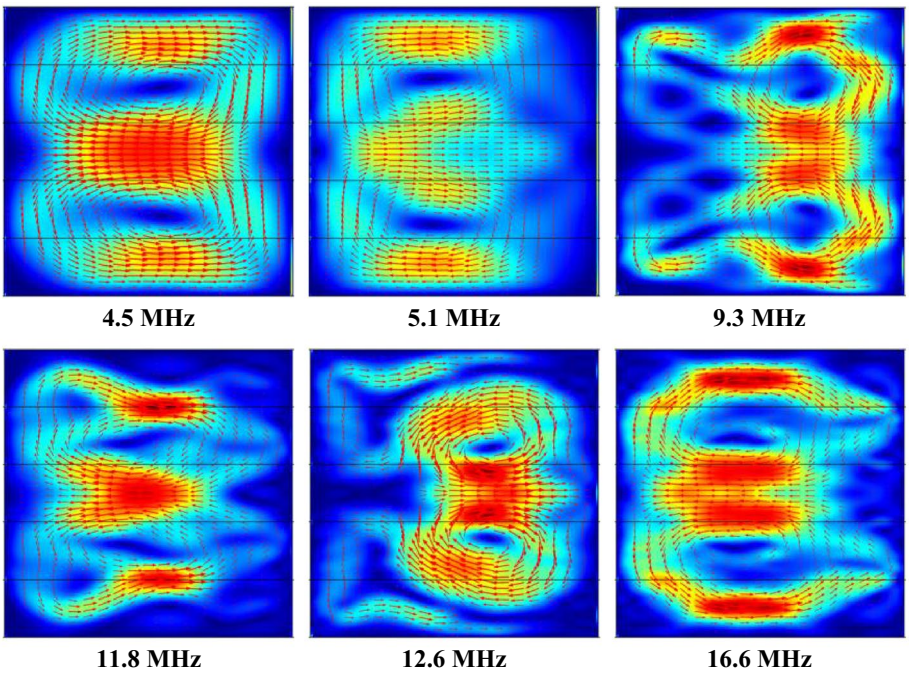

Fig. 8 Acoustofluidic fields generated by the defective phononic crystal plate obtained by removing the individual C-shaped ring element in the 3rd row and 6th column at different frequency points. **a** Frequency spectrum of transmission loss. **b** Patterns of sound intensity. **c** Patterns of acoustic streaming field in region 4

possibilities of considering phononic crystal structures as an effective element to customize ultrasonic field for constituting plentiful acoustofluidic devices in the investigation areas of rapid microfluidic mixing on a disposable chip and contactless manipulation of bio-organisms or micro-/nano-scale objects in a miniaturized total analysis system.

Fig. 8 (continued)

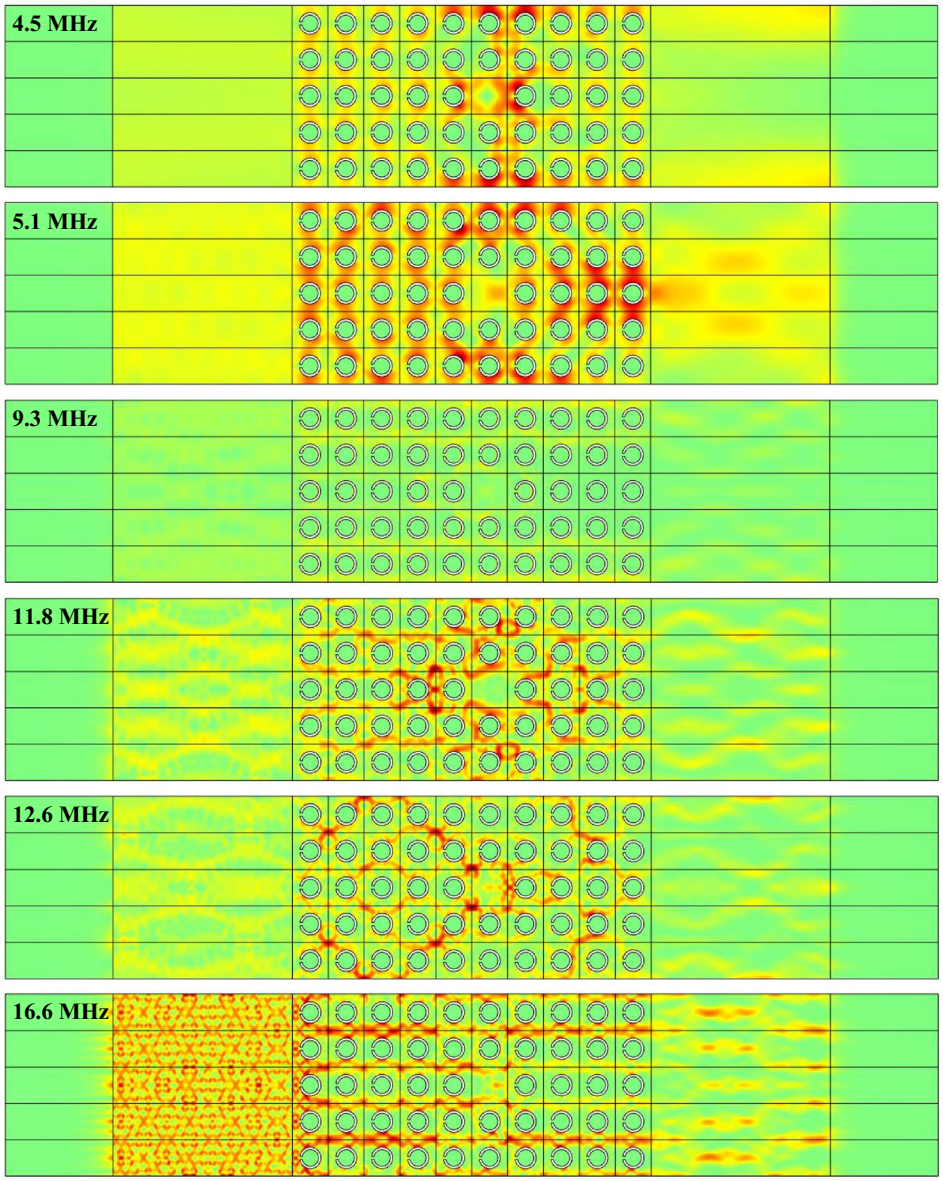

(b)

Acknowledgements This work was supported by the following funding organizations in China: The Natural Science Foundation of China (Grant no. 11904117, 51702113), the Industry-University-Research Collaboration Project of Jiangsu Province (Grant no. BY2019058), the Qing Lan Project of the Higher Educations of Jiangsu Province of China (2018), and the Scientific Research Foundation of Huaiyin Institute of Technology (Grant no. Z301B19529).

References

Ahmed D, Ozcelik A, Bojanala N, Nama N, Upadhyay A, Chen Y, Hanna-Rose W, Huang TJ (2016) Rotational manipulation of single cells and organisms using acoustic waves. Nat Commun 7:11085

Bourquin Y, Reboud J, Wilson R, Cooper JM (2010) Tuneable surface acoustic waves for fluid and particle manipulations on disposable chips. Lab Chip 10(15):1898–1901

Bourquin Y, Wilson R, Zhang Y, Reboud J, Cooper JM (2011) Phononic crystals for shaping fluids. Adv Mater 23(12):1458–1462

Bruus H (2012b) Acoustofluidics 2: perturbation theory and ultrasound resonance modes. Lab Chip 12(1):20–28

Bruus H (2012a) Acoustofluidics 7: the acoustic radiation force on small particles. Lab Chip 12(6):1014–1021

Cai F, He Z, Liu Z, Meng L, Cheng X, Zheng H (2011) Acoustic trapping of particle by a periodically structured stiff plate. Appl Phys Lett 99:253505

Chen J, Cong H, Loo FC, Kang Z, Tang M, Zhang H, Wu SY, Kong SK, Ho HP (2016) Thermal gradient induced tweezers for the manipulation of particles and cells. Sci Rep 6:35814

Connacher W, Zhang N, Huang A, Mei J, Zhang S, Gopesh T, Friend J (2018) Micro/nano acoustofluidics: materials, phenomena, design, devices, and applications. Lab Chip 18(14):1952–1996

Dai H, Xia B, Yu D (2019) Acoustic patterning and manipulating microparticles using phononic crystal. J Phys D Appl Phys 52:425302

Dai H, Chen T, Jiao J, Xia B, Yu D (2019) Topological valley vortex manipulation of microparticles in phononic crystals. J Appl Phys 126:145101

Dalili A, Samiei E, Hoorfar M (2018) A review of sorting, separation and isolation of cells and microbeads for biomedical applications: microfluidic approaches. Analyst 144(1):87–113

Destgeer G, Sung HJ (2015) Recent advances in microfluidic actuation and micro-object manipulation via surface acoustic waves. Lab Chip 15(13):2722–2738

Di Carlo D (2009) Inertial microfluidics. Lab Chip 9(21):3038–3046

Ehrnström R (2002) Miniaturization and integration: challenges and breakthroughs in microfluidics. Lab Chip 2(2):26N-30N

Elford DP, Chalmers L, Kusmartsev FV, Swallowe GM (2011) Matryoshka locally resonant sonic crystal. J Acoust Soc Am 130(5):2746–2755

Feng D, Xu DH, Xiong B, Wang YL (2015) Acoustically driven microfluidic devices based on hexagonal phononic crystal structures. In: 18th International conference on solid-state sensors, actuators and microsystems, pp 692–695

Folch A (2012) Introduction to BioMEMS. CRC Press, Boca Raton

Frank AG (2013) The future of microfluidic point-of-care diagnostic devices. Bioanalysis 5(1):1–3

Friend J, Yeo LY (2011) Microscale acoustofluidics: microfluidics driven via acoustics and ultrasonics. Rev Mod Phys 83(2):647–687

Hao N, Liu P, Bachman H, Pei Z, Zhang P, Rufo J, Wang Z, Zhao S, Huang TJ (2020) Acoustofluidics-assisted engineering of multifunctional three-dimensional zinc oxide nanoarrays. ACS Nano 14:6150–6163

Hsu JC, Lin YD (2019) Microparticle concentration and separation inside a droplet using phononic-crystal scattered standing surface acoustic waves. Sens Actuat A Phys 300(1):111651

Hu J (2014) Ultrasonic micro/nano manipulations: principles and examples. World Scientific Publishing, Singapore

Hussein MI, Leamy MJ, Ruzzene M (2014) Dynamics of phononic materials and structures: historical origins, recent progress, and future outlook. Appl Mech Rev 66(4):040802

Jericho SK, Jericho MH, Hubbard T, Kujath M (2004) Micro-electromechanical systems microtweezers for the manipulation of bacteria and small particles. Rev Sci Instrum 75(5):1280–1282

Jiang C, Liu X, Liu J, Mao Y, Marston PL (2017) Acoustic radiation force on a sphere in a progressive and standing zero-order quasi-Bessel-Gauss beam. Ultrasonics 76:1–9

Kanno Y, Tsuruta K, Fujimori K, Fukano H, Nogi S (2013) Phononic-crystal acoustic lens by design for energy-transmission devices. Electr Commun Jpn 97(1):22–27

Karlsen JT, Bruus H (2015) Forces acting on a small particle in an acoustical field in a thermoviscous fluid. Phys Rev E 92(4):043010

Ke M, Liu Z, Pang P, Wang W, Cheng Z, Shi J, Zhao X (2006) Highly directional acoustic wave radiation based on asymmetrical two-dimensional phononic crystal resonant cavity. Appl Phys Lett 88:263505

Kim SJ, Yokokawa R, Lesher-Perez SC, Takayama S (2015) Multiple independent autonomous hydraulic oscillators driven by a common gravity head. Nat Commun 6:7301

Kotz KT, Noble KA, Faris G (2004) Optical microfluidics. Appl Phys Lett 85(13):2658–2660

Lam KH, Li Y, Li Y, Lim HG, Zhou Q, Shung KK (2016) Multifunctional single beam acoustic tweezer for non-invasive cell/organism manipulation and tissue imaging. Sci Rep 6:37554

Lei J (2017) Formation of inverse Chladni patterns in liquids at microscale: roles of acoustic radiation and streaming-induced drag forces. Microfluid Nanfluid 21:50

Lei J, Glynne-Jones P, Hill M (2017) Comparing methods for the modelling of boundary-driven streaming in acoustofluidic devices. Microfluid Nanofluid 21:23

Lei J, Hill M, de León P, Albarrán C, Glynne-Jones P (2018) Effects of micron scale surface profiles on acoustic streaming. Microfluid Nanofluid 22:140

Lighthill J (1978a) Acoustic streaming. J Sound Vib 61(3):391–418

Lighthill J (1978b) Waves in fluids. Cambridge University Press, Cambridge

Lin SCS, Mao X, Huang TJ (2012) Surface acoustic wave (SAW) acoustophoresis: now and beyond. Lab Chip 12(16):2766–2770

Lisowski P, Zarzycki PK (2013) Microfluidic paper-based analytical devices (μPADs) and micro total analysis systems (μTAS): development. Appl Future Trends Chromatogr 76(19–20):1201–1214

Liu Z, Zhang X, Mao Y, Zhu YY, Yang Z, Chan CT, Sheng P (2000) Locally resonant sonic materials. Science 289(5485):1734–1736

Li S, Li M, Bougot-Robin K, Cao W, Chau IYY, Li W, Wen W (2013) High-throughput particle manipulation by hydrodynamic, electrokinetic, and dielectrophoretic effects in an integrated microfluidic chip. Biomicrofluidics 7(2):024106

Li F, Cai F, Liu Z, Meng L, Qian M, Wang C, Cheng Q, Qian M, Liu X, Wu J, Li J, Zheng H (2014) Phononic-crystal-based acoustic sieve for tunable manipulations of particles by a highly localized radiation force. Phys Rev Appl 1:051001

Li H, Wang Y, Ke M, Peng S, Liu F, Qiu C, Liu Z (2018) Acoustic manipulating of capsule-shaped particle assisted by phononic crystal plate. Appl Phys Lett 112:223501

Li F, Yan F, Chen Z, Lei J, Yu J, Chen M, Zhou W, Meng L, Niu L, Wu J, Li J, Cai F, Zheng H (2018) Phononic crystal-enhanced near-boundary streaming for sonoporation. Appl Phys Lett 113:083701

Li F, Xiao Y, Lei J, Xia X, Zhou W, Meng L, Niu L, Wu J, Li J, Cai F, Zheng H (2018) Rapid acoustophoretic motion of microparticles manipulated by phononic crystals. Appl Phys Lett 113:173503

Li F, Xia X, Deng Z, Lei J, Shen Y, Lin Q, Zhou W, Meng L, Wu J, Cai F, Zheng H (2019) Ultrafast rayleigh-like streaming in a sub-wavelength slit between two phononic crystal plates. J Appl Phys 125:134903

Li F, Cai F, Zhang L, Liu Z, Li F, Meng L, Wu J, Li J, Zhang X, Zheng H (2020) Phononic-crystal-enabled dynamic manipulation of microparticles and cells in an acoustofluidic channel. Phys Rev Appl 13:044077

Luong TD, Nguyen NT (2010) Surface acoustic wave driven microfluidics—a review. Micro Nanosyst 2(3):217–225

Lu X, Soto F, Li T, Liang Y, Wang J (2017) Topographical manipulation of microparticles and cells with acoustic microstreaming. ACS Appl Mater Interfaces 9(44):38870–38876

Lu X, Shen H, Zhao K, Wang Z, Peng H, Liu W (2019) Micro-/nanomachines driven by ultrasonic power sources. Chem Asian J 14(14):2406–2416

Mitri FG (2015) Acoustical tweezers using single spherically focused piston, X-cut, and Gaussian beams. IEEE Trans Ultrason Ferroelectr Freq Control 62(10):1835–1844

Muller PB, Barnkob R, Jensen MJH, Bruus H (2012) A numerical study of microparticle acoustophoresis driven by acoustic radiation forces and streaming-induced drag forces. Lab Chip 12(22):4617–4627

Ohno K, Tachikawa K, Manz A (2010) Microfluidics: applications for analytical purposes in chemistry and biochemistry. Electrophoresis 29(22):4443–4453

Qiu C, Xu S, Ke M, Liu Z (2014) Acoustically-induced strong interaction between two periodically patterned elastic plates. Phys Rev B 90:094109

Reboud J, Wilson R, Zhang Y, Ismail MH, Bourquin Y, Cooper JM (2012) Nebulisation on a disposable array structured with phononic lattices. Lab Chip 12(7):1268–1273

Reboud J, Bourquin Y, Wilson R, Pall GS, Jiwaji M, Pitt AR, Graham A, Waters AP, Cooper JM (2012) Shaping acoustic fields as a toolset for microfluidic manipulations in diagnostic technologies. Proc Natl Acad Sci USA 109(38):15162–15167

Reverté L, Prieto-Simón B, Campàs M (2016) New advances in electrochemical biosensors for the detection of toxins: nanomaterials, magnetic beads and microfluidics systems. A review. Anal Chim Acta 908:8–21

Sadhal SS (2012) Acoustofluidics 13: analysis of acoustic streaming by perturbation methods. Lab Chip 12(13):2292–2300

Srinivasan V, Pamula VK, Fair RB (2004) An integrated digital microfluidic lab-on-a-chip for clinical diagnostics on human physiological fluids. Lab Chip 4(4):310–315

Stone HA, Kim S (2001) Microfluidics: basic issues, applications, and challenges. AIChE J 47(6):1250–1254

Tang Q, Hu J (2015) Diversity of acoustic streaming in a rectangular acoustofluidic field. Ultrasonics 58:27–34

Tang Q, Wang X, Hu J (2017) Nano concentration by acoustically generated complex spiral vortex field. Appl Phys Lett 110:104105

Tang Q, Liu P, Hu J (2018) Analyses of acoustofluidic field in ultrasonic needle-liquid-substrate system for micro-/nanoscale material concentration. Microfluid Nanfluid 22:46

Tang Q, Zhou S, Huang L, Chen Z (2019) Diversity of 2D acoustofluidic fields in an ultrasonic cavity generated by multiple vibration sources. Micromachines (Basel) 10(12):803

Tang Q, Liang F, Huang L, Zhao P, Wang W (2020) On-chip simultaneous rotation of large-scale cells by acoustically oscillating bubble array. Biomed Microdevices 22(1):13

Temiz Y, Lovchik RD, Kaigala GV, Delamarche E (2015) Lab-on-a-chip devices: how to close and plug the lab? Microelectron Eng 132:156–175

Wang T, Ke M, Xu S, Feng J, Qiu C, Liu Z (2015) Dexterous acoustic trapping and patterning of particles assisted by phononic crystal plate. Appl Phys Lett 106:163504

Wang T, Ke M, Li W, Yang Q, Qiu C, Liu Z (2016) Particle manipulation with acoustic vortex beam induced by a brass plate with spiral shape structure. Appl Phys Lett 109:123506

Wang T, Ke M, Qiu C, Liu Z (2016) Particle trapping and transport achieved via an adjustable acoustic field above a phononic crystal plate. J Appl Phys 119:214502

Whitesides GM (2006) The origins and the future of microfluidics. Nature 442(7101):368–373

Wiklund M (2012) Acoustofluidics 12: biocompatibility and cell viability in microfluidic acoustic resonators. Lab Chip 12(11):2018–2028

Wiklund M, Green R, Ohlin M (2012) Acoustofluidics 14: applications of acoustic streaming in microfluidic devices. Lab Chip 12(14):2438–2451

Wilson R, Reboud J, Bourquin Y, Neale SL, Zhang Y, Cooper JM (2011) Phononic crystal structures for acoustically driven microfluidic manipulations. Lab Chip 11(2):323–328

Xia X, Yang Q, Li H, Ke M, Peng S, Qiu C, Liu Z (2017) Acoustically driven particle delivery assisted by a graded grating plate. Appl Phys Lett 111:031903

Xu S, Qiu C, Ke M, Liu Z (2014) Tunable enhancement of the acoustic radiation pressure acting on a rigid wall via attaching a metamaterial slab. Europhys Lett 105(6):64004

Yamada M, Seki M (2005) Hydrodynamic filtration for on-chip particle concentration and classification utilizing microfluidics. Lab Chip 5(11):1233–1239

Zheng LY, Wu Y, Ni X, Chen ZG, Lu MH, Chen YF (2014) Acoustic cloaking by a near-zero-index phononic crystal. Appl Phys Lett 104:161904

Zhou T, Deng Y, Zhao H, Zhang X, Shi L, Joo SW (2018) The mechanism of size-based particle separation by dielectrophoresis in the viscoelastic flows. J Fluids Eng 140:091302